Opto-electronic properties and solar cell efficiency modelling of Cu2ZnXS4 (X = Sn, Ge, Si) kesterites

Peer-reviewed author version

Raty, JY; BRAMMERTZ, Guy; VERMANG, Bart; Nguyen, ND & Ratz, T (2021)
Opto-electronic properties and solar cell efficiency modelling of Cu2ZnXS4 (X = Sn, Ge, Si) kesterites. In: JOURNAL OF PHYSICS-ENERGY, 3 (3) (Art N° 035005).

DOI: 10.1088/2515-7655/abefbe
Handle: http://hdl.handle.net/1942/35859

Opto-electronic properties and solar cell efficiency modelling of Cu_2ZnXS_4 (X=Sn,Ge,Si) kesterites*

Thomas Ratz,[1,2] Jean-Yves Raty,[1,3] Guy Brammertz,[4] Bart Vermang,[2,4,5] and Ngoc Duy Nguyen[1]

[1] *CESAM / Q-MAT / Solid State Physics, Interfaces and Nanostructures, Physics Institute B5a, Allée du Six Août 19, B-4000 Liège, Belgium*

[2] *Institute for Material Research (IMO), Hasselt University, Agoralaan gebouw H, B-3590 Diepenbeek, Belgium*

[3] *University of Grenoble Alpes / CEA-LETI / MINATEC Campus / Rue des Martyrs 17, F-38054 Cedex 9 Grenobles, France*

[4] *IMEC division IMOMEC / partner in Solliance, Wetenschapspark 1, B-3590 Diepenbeek, Belgium*

[5] *Energyville, Thor Park 8320, B-3600 Genk, Belgium*

(Dated: June 15, 2021)

In this work, first-principles calculations of Cu_2ZnSnS_4, Cu_2ZnGeS_4 and Cu_2ZnSiS_4 are performed to highlight the impact of the cationic substitution on the structural, electronic and optical properties of kesterite compounds. Direct bandgaps are reported with values of 1.32, 1.89 and 3.06 eV respectively for Cu_2ZnSnS_4, Cu_2ZnGeS_4 and Cu_2ZnSiS_4 and absorption coefficients of the order of 10^4 cm^{-1} are obtained, indicating the applicability of these materials as absorber layer for solar cell applications. In the second part of this study, *ab initio* results are used as input data to model the electrical power conversion efficiency of kesterite-based solar cells. In that perspective, we used an improved version of the Shockley-Queisser model including non-radiative recombination via an external parameter defined as the internal quantum efficiency. Based on predicted optimal absorber layer thicknesses, the variation of the solar cell maximal efficiency is studied as a function of the non-radiative recombination rate. Maximal efficiencies of 25.71, 19.85 and 3.10 % are reported respectively for Cu_2ZnSnS_4, Cu_2ZnGeS_4 and Cu_2ZnSiS_4 for vanishing non-radiative recombination rate. Using an internal quantum efficiency value providing experimentally comparable V_{OC} values, cell efficiencies of 15.88, 14.98 and 2.66 % are reported respectively for Cu_2ZnSnS_4, Cu_2ZnGeS_4 and Cu_2ZnSiS_4. We confirm the suitability of Cu_2ZnSnS_4 in single junction solar cells, with a possible efficiency improvement of nearly 10% enabled through the reduction of the non-radiative recombination rate. In addition, Cu_2ZnGeS_4 appears to be an interesting candidate as top cell absorber layer for tandem approaches whereas Cu_2ZnSiS_4 might be interesting for transparent photovoltaic windows.

Introduction

Over the years, photovoltaic (PV) thin film technology has emerged as an interesting candidate for efficient and large-scale energy production. To this aim, this technology must fulfill several criteria such as low-cost thin film synthesis, high solar cell efficiency and materials resources availability and accessibility [1]. In relation with the latter point, the European Commission has identified Ga and In as critical raw materials and highlighted the scarcity of those elements used for the synthesis of inorganic chalcogenide $CuInGa(S,Se)_2$ (CIGS) alloys implemented as absorber layer for PV applications [2]. Despite the high efficiency reported for CIGS solar cells, with a record value of 23.3% [3, 4], the incorporation of this material in a large-scale energy production technology might be compromised. This justifies an urgent search for alternative compositions with comparable or better efficiencies than CIGS. As a consequence, over the past 20 years, the scientific community has been investigating kesterite $Cu_2ZnSn(S,Se)_4$ materials as absorber layer in solar cell applications [5]. Benefiting from the well-established knowledge of CIGS, kesterite-based solar cell efficiency gradually increased over the years, reaching values of 12.6% for $Cu_2ZnSn(S,Se)_4$ [6] and 11% for Cu_2ZnSnS_4 [7] using various chemical [8] or physical [9] routes for the synthesis of the kesterite thin films.

However, new challenges concerning further efficiency improvements have recently arisen. Large open circuit voltage V_{OC} deficits have been reported as responsible for the efficiency limitation encountered [5, 10]. Several elements have been pointed out as possible culprits for the V_{OC} deficits, including interface recombination due to bands misalignment [11, 12], formation of secondary phases, and/or high intrinsic point defect concentration leading to non-radiative recombination in the kesterite bulk material [13, 14]. As a result, recombination centres are present both at the architectural level (band misalignments with the buffer layer) and at the compositional/morphological level (defects and/or secondary phases) within the absorber layer. Focusing on the kesterite absorber layer, several solution paths have been considered to overcome the current efficiency limitation, like alloying using isoelectronic substitution elements such as Ag for Cu, Ge for Sn or Se for S [15, 16] or via the cationic substitution of Zn or Sn [17, 18].

In the past, alternative kesterite materials have been studied both theoretically and experimentally, leading to promising efficiencies for Ge-containing kesterite compounds [19–24]. Using density functional theory (DFT) calculations, a few works reported predictions over structural properties, electrical properties or optical properties of alternative kesterite materials such as Cu_2ZnSnS_4 [25–31], Cu_2ZnGeS_4 [25–27, 32, 33] and Cu_2ZnSiS_4 [25–27]. However, the variety of computational approaches do not facilitate the comparison of the materials physical properties. In addition, to the best of our knowledge, the DFT results are rarely compared to experimental measurements.

In this work, we first investigate theoretically the cationic substitution of Sn by two other iso-electronic elements: Ge and Si, in kesterite Cu_2ZnSnS_4. The structural and opto-electronic properties are calculated for Cu_2ZnSnS_4 as the reference material [9], Cu_2ZnGeS_4 as a promising material regarding the experimental efficiency achieved [9, 23] and Cu_2ZnSiS_4 as an interesting candidate regarding the elemental abundance [1]. Then, the obtained *ab initio* results are used as input data to feed an improved version of the Shockley-Queisser model [34], allowing us to connect the intrinsic material properties to the solar cell macroscopic properties. Via this cell efficiency modelling, physical quantities such as the open circuit voltage V_{OC}, the short circuit current density J_{SC} and the fill factor FF are computed.

In the first section of this paper, the structural properties of the materials are presented. Then, in the following sections, the Heyd–Scuseria–Ernzerhof exchange-correlation functional (HSE06) [35] is used to compute the electronic and optical properties. Based on the band structures and the densities of states (DOS), the electrical properties of the materials are reported and compared. To complete the investigation, the optical properties are presented and related to the electrical ones. This approach allows us to extract the general trends highlighting the impact of the cationic substitution of Sn by Ge and Si on the opto-electronic properties. In the second part of this work, using the *ab initio* results as input data, the upper limit of the kesterite-based solar cell efficiency is calculated using the theoretical model proposed by Blank *et.al.* [36]. This model allows us to compute physical quantities that can be compared to experimental results such as the solar cell efficiency η using as parameters the solar cell temperature T, the absorber layer thickness d and the internal quantum efficiency Q_i.

Computational method

First-principles calculations have been performed using Vienna *Ab initio* Simulation Package (VASP) code [37] with the Projector-Augmented Wave (PAW) potential method [38]. Perdew-Burke-Ernzerhof (PBE) GGA pseudo-potentials [39] were used with the following valence electrons considered for each element: Cu: $3d^{10}4s^1$, Zn: $3d^{10}4s^2$, Sn: $4d^{10}5s^25p^2$, Ge: $3d^{10}4s^24p^2$, Si: $3s^23p^2$ and S: $3s^23p^4$. Ionic and electronic relaxation were achieved using a cut-off energy of 550 eV and a Γ-centered uniform **k**-points mesh of $6 \times 6 \times 6$ **k**-points. Applying the strongly constrained and appropriately normed semilocal density functional (SCAN) [40, 41], the structures were relaxed until the numerical convergence regarding the self-consistent cycles reaches forces between ions less than 10^{-3} eV/Å. The system total energy was converged down to 10^{-6} eV. During relaxation, the symmetry was kept constant to the kesterite point group symmetry ($I-4$) and the atomic positions, cell volume and cell shape were allowed to relax. The SCAN meta-GGA functional was proven effective to predict improved geometries for a computational cost comparable to the GGA functional. Moreover, Fritsch *et.al.* reported that the combination of SCAN functional calculations for ionic relaxations followed by a single HSE06 functional electronic calculation provides accurate results for kesterite materials [42]. Consequently, starting from the relaxed structure, the HSE06 exchange-correlation functional, known for its bandgap prediction accuracy [43], was used to compute the electronic and optical properties. Concerning the optical calculations, the imaginary part of the dielectric tensor was first obtained via a sum over states by applying the Fermi golden rule between valence band and conduction band states at a given **k**-point. Then, the real part of the dielectric tensor was obtained thanks to a Kramers-Kroning transformation for which the convergence was properly ensured via a sufficiently high number of conduction band energy levels included in the calculation.

Results and discussion

Structural properties

The lattice parameters a, b, c (*cfr.* Fig.1), the conventional cell volume V and the atomic distances $d_{\mathrm{Cu-S}}$ and $d_{\mathrm{X-S}}$ (X=Sn,Ge,Si) were obtained as a result of the ionic relaxation (see Table 1).

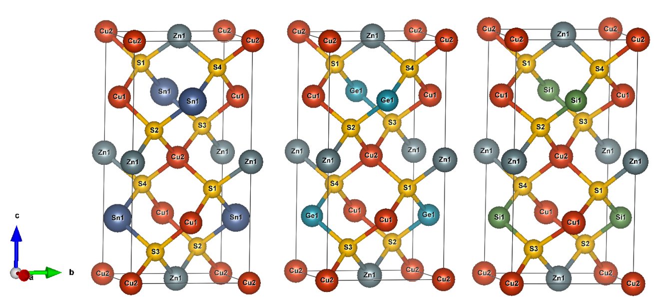

Figure 1. Representation of the conventional cells of the Cu_2ZnXS_4 (X=Sn,Ge,Si) kesterites.

The sequential substitution of Sn by Ge and Si induces a contraction of the kesterite lattice parameters. A reduction of a and b from 5.40 Å (Cu_2ZnSnS_4) to 5.25 Å (Cu_2ZnSiS_4) is observed while the c parameter is reduced from 10.79 Å to 10.32 Å. The results reported in Table 1 are in good agreement with experimental measurements for Cu_2ZnSnS_4 [44–49] and Cu_2ZnGeS_4 [47, 49–51]. To our knowledge, experimental characterisation of Si-pure kesterite crystal structures has not been reported yet. According to Refs. [52, 53], an orthorhombic crystalline structure is observed for high Si concentrations. Nevertheless, several theoretical works [26, 27] reported values close to $a, b = 5.25$ Å and $c = 10.32$ Å as obtained here. This lattice contraction can be interpreted by taking into account the successive reduction of the atomic radius of the substitutional cation from $r_{Sn} = 1.45$ Å, to $r_{Ge} = 1.25$ Å and to $r_{Si} = 1.10$ Å [54]. Consequently, the conventional cell volume decreases from 314.9 $Å^3$ for the Sn-containing compound to 294.87 $Å^3$ for Cu_2ZnGeS_4 and to 283.94 $Å^3$ for Cu_2ZnSiS_4. One can also notice that the cation substitution does not impact the $d_{\mathrm{Cu-S}}$ distances. In the following section, the results presented here will be put into perspective with the electronic properties.

Materials	Ref. (Type)	a,b [Å]	c [Å]	V [Å^3]	$d_{\mathrm{X-S}}$ [Å]	$d_{\mathrm{Cu-S}}$ [Å]
Cu_2ZnSnS_4	This work.	5.40	10.79	314.90	2.44	2.29
	[44] (Exp.)	5.67	11.30			
	[45] (Exp.)	5.42	10.79		2.39	2.33
	[46] (Exp.)	5.42	10.79			
	[47] (Exp.)	5.43	10.86			
	[48] (Exp.)	5.43	10.86			
	[49] (Exp.)	5.42	10.86			
	[26] (Theo.)	5.44	10.76			
	[28] (Theo.)	5.33	10.66			
	[29] (Theo.)	5.47	10.92			
	[27] (Theo.)	5.45				
	[30] (Theo.)	5.43	10.86			
	[31] (Theo.)	5.45	10.89			
Cu_2ZnGeS_4	This work.	5.30	10.51	294.87	2.26	2.28
	[47] (Exp.)	5.34	10.57			
	[49] (Exp.)	5.28	10.71			
	[50] (Exp.)	5.33-5.34	10.52-10.59	299.54-301.95		
	[51] (Exp.)	5.30-5.37	10.49-10.69			
	[26] (Theo.)	5.28	10.49			
	[27] (Theo.)	5.35				
	[32] (Theo.)	5.35	10.49			
	[33] (Theo.)	5.38	10.49			
Cu_2ZnSiS_4	This work.	5.25	10.32	283.94	2.15	2.28
	[26] (Theo.)	5.22	10.30			
	[27] (Theo.)	5.31				

Table 1. Lattice parameters a, b and c (see Fig. 1) and conventional cell volume V of Cu_2ZnXS_4 (X=Sn,Ge,Si) kesterites. Interatomic distances between the cation (X=Sn,Ge,Si) and the sulphur atom $d_{\mathrm{X-S}}$ are reported as well as the copper-sulphur distances $d_{\mathrm{Cu-S}}$. Empty cells denote the absence of available data.

Electronic properties

As it can be observed in Fig. 2, all calculated kesterite bands present a direct bandgap located at the Γ point. Using an approach similar to that reported in Refs. [25–27], the bandgap values reported in Table 2 were obtained from the energy differences between the conduction band minimum and the valence band maximum energy levels as extracted from the Kohn-Sham eigenvalues. As reported in Table 2, the bandgap energy E_G increases from 1.32 eV for Cu_2ZnSnS_4 to 1.89 eV for Cu_2ZnGeS_4 and to 3.06 eV for Cu_2ZnSiS_4. These results are comparable to those reported by Zamulko *et.al.* in their theoretical investigation [26]. In comparison to experimental values, the Sn-containing kesterite bandgap is underestimated by 0.18 eV as usual reported values are around 1.5 eV [9]. In contrast, the Cu_2ZnGeS_4 bandgap value of 1.89 eV fits with the reported experimental bandgaps with values between 1.88 and 2.25 eV [49–51, 55–57]. According to Ref. [58], a bandgap value of 2.71 eV was experimentally obtained for Cu_2ZnSiS_4.

We provide here a focus on the orbitals projected DOS and their contributions to electronic states in the band structure, for the Sn-kesterite compound (Fig. 2a). The main contributions to the conduction band states come from S 3p and Sn 5s atomic orbitals close to the bottom of the band and S 3p and Sn 5p atomic orbitals for higher energy levels. Concerning the valence band, the hybridisation between Cu 3d and S 3p orbitals provide the main contributions to energy states at the top of the band. These results are corroborated by the work of Paeir *et.al.* in Ref. [31]. This tendency is also observed for the two other kesterite materials, *i.e.* the bottom of the conduction band is formed by either the s atomic orbital of the cation X (X=Sn, Ge) or the p orbital of the cation Si and the 3p orbital of the chalcogen S, while the contributions to the top of the valence band come from the 3d atomic orbital of Cu and the 3p atomic orbital of the sulphur element.

For Cu_2ZnGeS_4 and Cu_2ZnSiS_4, the substitution of Sn by Ge and Si (Figs. 2b & 2c) seems to slightly flatten the energy level at the bottom of the conduction band. The bandgap increase from 1.32 to 3.06 eV is due to the variation of the chemical interaction between the cation and the sulphur, which leads to (i) a weak flattening of the energy level at the bottom of the conduction band and (ii) a shift of this energy level towards higher energies. To link those observations to the structural properties of the materials one can put into perspective the decrease of the cation/sulphur interatomic distance $d_{\mathrm{X-S}}$ with the increase of the kesterite bandgap. In contrast, the substitution of the cation atoms leaves the valence band unchanged as the orbitals contributing to these states are from Cu and S for which the interatomic distances $d_{\mathrm{Cu-S}}$ are reported constant from one kesterite material to an-

Materials	E_G [eV]	$m^*_{//}$ $[m_e]$				$m^*_{\perp}$ $[m_e]$				ϵ_∞ $[\epsilon_0]$
		$\Gamma_{v,1}$	$\Gamma_{v,2}$	$\Gamma_{v,3}$	Γ_c	$\Gamma_{v,1}$	$\Gamma_{v,2}$	$\Gamma_{v,3}$	Γ_c	
Cu_2ZnSnS_4	1.32 (This work) 1.50 [9] (Exp.) 1.26-1.77 [25, 26, 30, 31] (Theo.)	-0.69	-3.32	-0.16	0.19	-0.77	-0.64	-0.19	0.18	6.77
Cu_2ZnGeS_4	1.89 (This work) 1.88-2.25 [49–51, 55–57] (Exp.) 2.10-2.38 [25, 26, 30, 32] (Theo.)	-0.72	-3.49	-0.19	0.23	-0.72	-0.63	-0.24	0.22	6.44
Cu_2ZnSiS_4	3.06 (This work) 2.71 [58] (Exp.) 3.05 [25, 26] (Theo.)	-1.44	-3.65	-0.25	0.26	-1.63	-0.68	-0.33	0.25	5.78

Table 2. Bandgaps E_G and effective masses m^* scaled by the free electron mass m_0 of Cu_2ZnXS_4 (X=Sn,Ge,Si) kesterites. Effective masses have been calculated around the Γ high symmetry **k**-point and along two directions in the reciprocal space: [0,0,0] to [0,0,1] (resp. [0,0,0] to [0,1,0]) for the first effective mass component $m_\perp$ (resp. for the second component $m_{//}$) comparable to values reported in Ref. [27]. High-frequency dielectric constants ϵ_∞ of the materials are also presented and scaled with the vacuum electrical permittivity ϵ_0 comparable to values reported in Ref. [26].

other (*cfr.* Table 1).

In addition to the bandgaps, the effective masses are presented in Table 2. These ones have been calculated around the Γ point, at the direct bandgap location, and along two directions in the reciprocal space: [0,0,0] to [0,0,1] for the first effective mass component $m_\perp$ and along [0,0,0] to [0,1,0] for the second component $m_{//}$. As shown in Fig. 2, one energy level is present at the bottom of the conduction band and three energy levels are located at the top of the valence band. Consequently, the effective masses have been calculated for the lowest energy level in the conduction band named Γ_c and for the three highest energy levels at the top of the valence band $\Gamma_{v,1}$, $\Gamma_{v,2}$, $\Gamma_{v,3}$, labeled from the highest energy level to the lowest one. For both the conduction and valence band, the general trend observed is a slight increase of the effective mass absolute value, with only two occasions of exceptions (for $\Gamma_{v,1}$ and $\Gamma_{v,2}$ of the $m^*_\perp$ component), when Sn is sequentially substituted by Ge and Si. Then, as kesterite materials behave electrically as p-type semiconductor [10], we first discuss the hole effective mass values. As presented in Table 2, concerning the $m^*_{//}$ component, $\Gamma_{v,2}$ effective masses are significantly higher than $\Gamma_{v,1}$ and $\Gamma_{v,3}$, highlighting the presence of light and heavy holes in this particular direction. In addition, similar values are reported regarding $\Gamma_{v,1}$ and $\Gamma_{v,3}$ for the perpendicular component while, in contrast, $\Gamma_{v,2}$ is five times lower than in the parallel direction. Concerning the electron effective masses, similar values are obtained for both components $m^*_{//}$ and $m^*_\perp$ with a slight increase from a minimal value of 0.18 m_e to a maximal value of 0.26 m_e observed as the Sn cation is substituted. These values are in good agreement with those obtained by Liu *et.al.* with reported effective masses of 0.18, 0.21 and 0.26 m_e (resp. 0.19, 0.22, 0.24 m_e) in the parallel (resp. perpendicular) direction [27]. This suggests that the hole and electron effective masses would only slightly increase as Sn is substituted by Ge and then Si. In summary, the cationic substitution does not impact significantly the hole nor electron effective masses but leads to a significant increase of the kesterite bandgap.

Optical properties

Following the computation of the electronic properties, the optical properties of the kesterite materials have been determined via the calculation of the dielectric tensor $\epsilon(E)$ whose real ϵ_1 and imaginary ϵ_2 parts are shown in Fig. 3a (see supplementary material for the detailed equations). In this figure, the components xx, yy and zz of $\epsilon(E)$ are presented for each compound. It appears that the sequential substitution of Sn with Ge and Si leads to a decrease of the high frequency dielectric response ϵ_∞ from 6.77 ϵ_0 (Cu_2ZnSnS_4) to 6.44 ϵ_0 (Cu_2ZnGeS_4) and reaching 5.78 ϵ_0 for the Si-containing compound (*cfr.* Table 2). These results are comparable to the values of 6.7 (Cu_2ZnSnS_4), 6.6 (Cu_2ZnGeS_4) and 5.7 (Cu_2ZnSiS_4) reported by Zamulko *et.al.* in Ref. [26]. As expected, the decrease in ϵ_∞ is in agreement with the increase of the materials bandgap. Concerning the imaginary part of the dielectric tensor $\epsilon_2(E)$, the onset of absorption is also shifted towards higher energies as the bandgap increases. In addition, in Fig. 3a, one can notice that the peaks positions correspond well to the bandgaps reported in Table 2.

Then, the absorption coefficient $\alpha(E)$ as well as the reflectivity $R(E)$ and refractive index $n(E)$ are computed as described in the supplementary material. In Fig. 3b the absorption coefficient of the materials are presented alongside the solar irradiance spectrum. First, one can notice that the kesterite compounds exhibit absorption

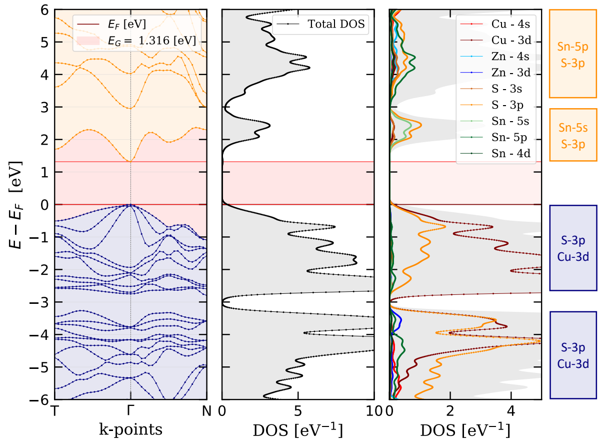

(a) Cu_2ZnSnS_4

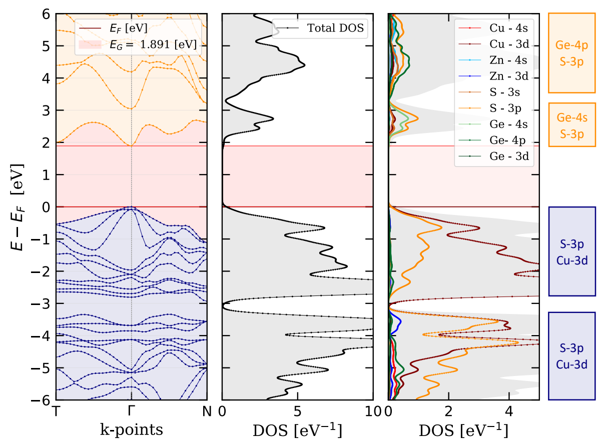

(b) Cu_2ZnGeS_4

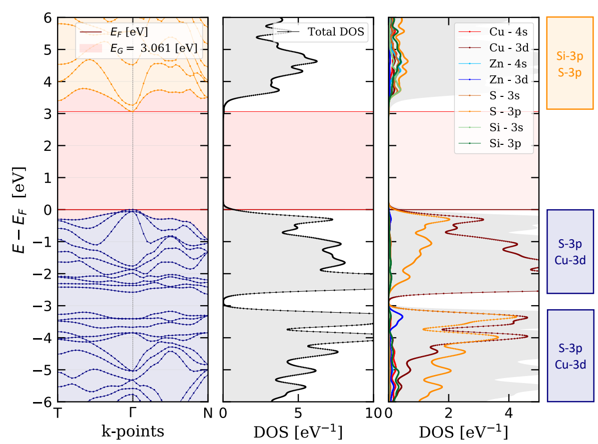

(c) Cu_2ZnSiS_4

Figure 2. Band structures, densities of states and orbital projected densities of states of Cu_2ZnXS_4 (X=Sn,Ge,Si) kesterites. The densities of states are presented with an applied gaussian smearing of 0.08 eV. The band dispersion is calculated along T: [0,0,1/2] - Γ: [0,0,0] - N: [1/2,1/2,1/2]. Main atomic orbital contributions to the DOS are presented alongside the figures.

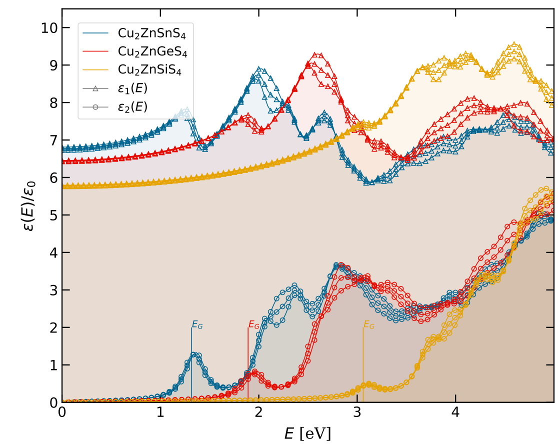

(a) Dielectric tensor

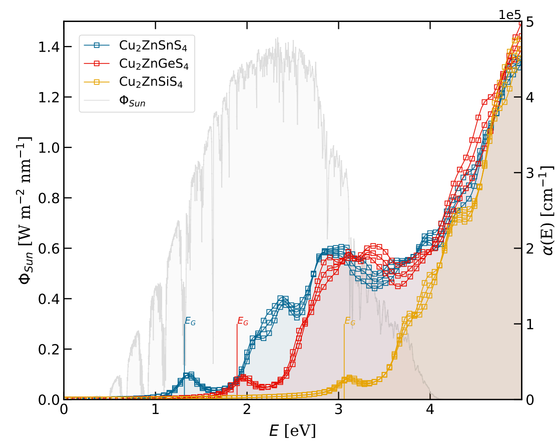

(b) Absorption coefficient

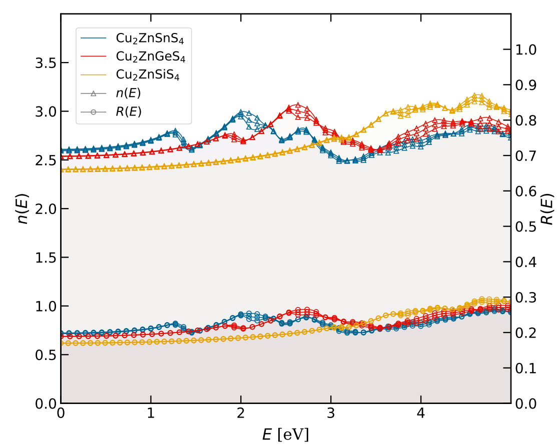

(c) Refractive index and reflectivity

Figure 3. (a) Real ϵ_1 and imaginary ϵ_2 parts of the dielectric tensor $\epsilon(E)$. For each compound, the xx, yy and zz components of the tensor are presented. (b) The absorption coefficients $\alpha(E)$ and the solar irradiance spectrum are presented. (c) Materials refractive indices $n(E)$ and reflectivity $R(E)$ spectra.

coefficient values between 0 and 2×10^5 cm^{-1} within the energy range of non-negligible solar irradiance (between 0.5 and 4 eV). This result highlights the applicability of these kesterite materials as absorber layer in solar cell applications. However, an energetic shift of the absorption curves is also observed from the Sn-containing kesterite to the Si-containing kesterite with a first absorption peak located at the respective bandgap energies of the materials. The Cu_2ZnSnS_4 and Cu_2ZnGeS_4 curves have a similar behaviour while for the Si-containing kesterite curve, the plateau observed for the two other kesterites disappears as a consequence of the energy level shift at the bottom of the conduction (*cfr.* Fig. 2c). Finally, in Fig. 3c, the refractive index $n(E)$ and reflectivity $R(E)$ are presented. As reported, the refractive indices at 0 eV are 2.59, 2.53 and 2.40 respectively for Cu_2ZnSnS_4, Cu_2ZnGeS_4 and Cu_2ZnSiS_4 with variations of 0.6 in values between 0 and 5 eV. Concerning the reflectivity values, a variation from 20 to 30% within the 0 to 5 eV energy range is observed. Additionally, it is worth noticing some reflectivity differences of nearly 10% between Cu_2ZnSnS_4 and Cu_2ZnSiS_4 for some energy values.

Electrical power conversion efficiency

In this section, we focus on the theoretical modelling of solar cell macroscopic physical quantities such as the short circuit current density J_{SC}, the open circuit voltage V_{OC} and the solar cell electrical power conversion efficiency η using Cu_2ZnXS_4 (X=Sn,Ge,Si) as absorber layer. The predictions are realised based on the theoretical model presented by Blank *et.al.* [36]. The improvements proposed by Blank *et.al.* over the Shockley-Queisser model [34] are (i) the use of the internal quantum efficiency Q_i as a model parameter to take into account non-radiative recombinations and (ii) the incorporation of light trapping by taking into account the refractive index $n(E)$ in the calculation of the radiative current density $J_{\mathrm{rad},0}(n,d)$ (see supplementary material).

Non-radiative recombination occur via recombination centres: intrinsic point defects, defect clusters and grain boundaries in the bulk material or also through recombination centres at the interfaces of the various layers composing the solar cell. As a consequence, these recombination centres have an impact on the solar cell properties. Therefore, in this theoretical work, we chose to use the non-radiative recombination rate as a model parameter. In that perspective, the internal quantum efficiency is expressed as the ratio between the radiative recombination rate $R_{\mathrm{rad},0}$ and the total recombination rate: $R_{\mathrm{rad},0} + R_{\mathrm{nrad},0}$, leading to a non-radiative recombination rate under equilibrium conditions,

$$R_{\mathrm{nrad},0} = R_{\mathrm{rad},0}\frac{(1-Q_i)}{Q_i} \quad (1)$$

Considering a perfectly crystalline material, all recombinations are radiative and the photons emitted (i.e., not reabsorbed) contribute to the emission spectrum of the material which, in this model, is assumed as the black body spectrum at temperature $T = 300$ K. These radiative recombinations are therefore thermodynamically required and are proportional to the amount of electrons within the conduction band (i.e., proportional to the temperature). This first situation corresponds to an internal luminescence quantum efficiency Q_i value equals to unity for which the total recombination rate R_0 is equal to the radiative recombination rate $R_{\mathrm{rad},0}$. In the case of recombination centres within the bulk materials or at the interfaces, both radiative and non-radiative recombination are included. The thermodynamic condition of emission must still be fulfilled ($R_{\mathrm{rad},0}$) and additionally, recombinations via recombination centres occur ($R_{\mathrm{nrad},0}$), leading to an increase of the total recombination rate R_0. In this paper, the Q_i value is related to the amount of non-radiative recombinations which is proportional to the number of radiative recombinations (Eq. (1)). Q_i can consequently be related to the internal quantum efficiency IQE which is an experimentally measured physical quantity. The detailed description of the theoretical model proposed by Blank *et.al.* is presented in the supplementary material. To feed this theoretical model we use the previously calculated optical results ($\alpha(E)$, $n(E)$ and $R(E)$) as input data. It is worth noticing that the computed material properties obtained correspond to a perfect crystal situation (i.e., $Q_i = 1$). As the internal quantum efficiency tends to vanish, variations of the optical properties are expected as defects will introduce new electronic states. However, in this work the perfect crystal optical properties are considered for each value of Q_i. Accordingly, the absorptance $A(E)$ of the absorber layer is determined via Eq. (2), assuming a flat solar cell surface and a thin film thickness d:

$$A(E,d) = [1 - R(E)] - \exp(-2\alpha(E)d) \quad (2)$$

The obtained results are presented for a solar cell temperature T=300K as follow:

- First, we evaluate the optimal thicknesses (i.e., associated to a maximum for η) of the absorber layer as a function of Q_i. To this perspective, the efficiency of the solar cell is calculated for different values of the absorber layer thickness d and for various internal quantum efficiency values $Q_i \in [10^{-6}; 1]$ (Fig. 4). The efficiencies were calculated using the materials reflectivity R(E) as obtained from the first-principles calculations.

- Using this optimal thickness, we compute the maximal efficiency for a range of internal quantum efficiency values $Q_i \in [10^{-6}; 1]$ (Fig. 5). In addition, to highlight the impact of the absorber layer reflectivity on the solar cell properties, the calculation is performed with and without taking into account the materials reflectivity $R(E)$ in the calculation of the absorptance $A(E)$ (Eq. (2)).

- Then, in Fig. 6, the current density voltage curves for the respective kesterite-based solar cells are presented for different internal quantum efficiency values $Q_i \in [10^{-6}; 1]$ and for a usual absorber layer thickness of 1.5 μm.

- In Table 3, the main solar cell electrical characteristics are reported first by assuming no non-radiative recombination (i. e., $Q_i = 1$) and secondly by assuming a non-radiative recombination rate fixed by $Q_i = 10^{-4}$ in order to obtain results comparable to actual experimental device characteristics (i. e., experimentally comparable V_{OC} values). Finally, the results obtained are compared to various experimental works.

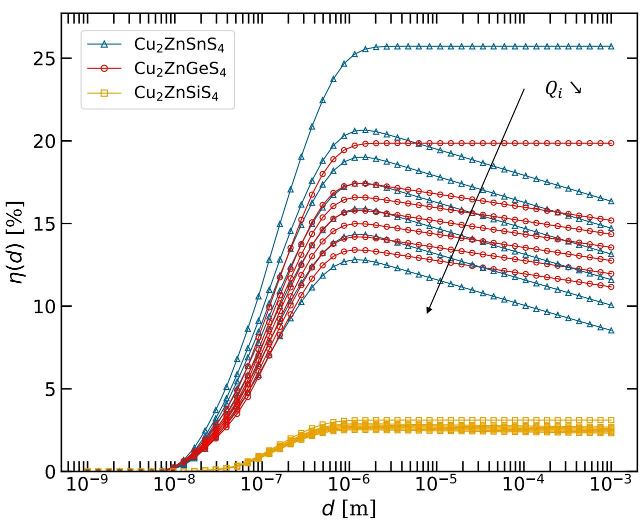

Figure 4. Solar cell efficiency modelling presented as a function of the absorber thin film thickness d for various internal quantum efficiency $Q_i \in [10^{-6}; 1]$. The efficiencies were calculated using the materials reflectivity R(E) as obtained from the first-principles calculations (*cfr.* Eq.(2))

In Fig. 4, the maximal efficiency is calculated as a function of the absorber layer thickness. Each curve represents an internal quantum efficiency value ranging logarithmically from 1 (highest efficiency) to 10^{-6} (lowest efficiency). Here, we report a significant disparity between the Cu_2ZnSiS_4-based solar cell efficiencies with values below 5% for all Q_i, compared to the cells based on the two other kesterite materials. This observation is linked to the larger bandgap of Cu_2ZnSiS_4, which limits drastically the short circuit current density (see supplementary material) as illustrated in Fig. 6 and Table 3. The general trend observed for all materials is an increase of the efficiency as the absorber thickness increases over 10 nm. Then, for d just above 1 μm, the efficiency reaches a plateau, for $Q_i = 1$, with maximal efficiency values of 25.71, 19.85 and 3.1 % respectively for the Sn-, Ge- and Si-kesterite compound. In contrast, for $Q_i < 1$, the efficiencies reach a maximal value for an optimal thickness before decaying linearly as d increases. The optimal thicknesses reported for the absorber layer thin films are between 1.15 and 2.68 μm (*cfr.* Table 3). The observed increase of η with d can be explained by the optimisation of the the absorptance function $A(E)$ which gets closer to $1 - R(E)$ for $E > E_G$, thus maximising the short circuit current density. The optimisation of the absorptance also maximises $J_{\mathrm{rad},0}$ which reduces V_{OC} and reduces η but this phenomenon is not dominant here. Then, for a unit value of Q_i, J_{SC} asymptotically reaches a maximum value and any further increase of the thickness (over the optimal thickness value) does not result in any notable increase of the efficiency value. In contrast, for internal quantum efficiency values $Q_i < 1$, as the absorber layer gets thicker, the non-radiative recombination rate increases, leading to a decrease of the open circuit voltage and, consequently, to the efficiency drop (see supplementary material).

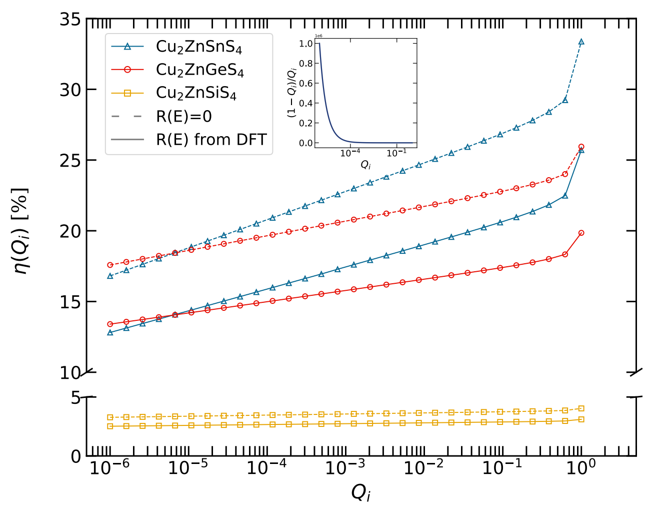

Figure 5. Solar cell efficiency modelling for an optimal absorber layer thickness extracted from Fig. 4 presented as a function of the internal quantum efficiency $Q_i \in [10^{-6}; 1]$. Results from simulations taking into account the materials reflectivity $R(E)$ are presented in full lines while dashed lines represent the maximal efficiencies obtained assuming $R(E) = 0$. In inset, evolution of the prefactor fixing the non-radiative recombination rate as described in Eq. (1) with respect of Q_i.

From the previous calculations, for each Q_i value, the absorber layer thickness giving the maximum efficiency is extracted as the optimal absorber thickness value d_{opt}. Then, in a second calculation (Fig. 5), the evolution of the maximal efficiency as a function of the internal quantum efficiency for an optimal thickness is reported both without (dashed lines, $R(E) = 0$) and with (full lines, $R(E)$ from DFT results in section) taking into account the materials reflectivity in the absorptance calculation (see Eq. (2)). Concerning the impact of the materials reflectivity on the solar cell efficiency for the Cu_2ZnSnS_4 compound, depending on the Q_i value, a percentage point loss of 4 to 8 in efficiency is observed (decrease of 4 to 6 observed for Cu_2ZnGeS_4 and of 1 for Cu_2ZnSiS_4). Concerning the behaviour of η with respect to Q_i, the cell efficiency increases as Q_i tends to unity and as the non-radiative recombination rate decays towards 0 (see Eq. (1)). Then, as the internal quantum efficiency decreases, the efficiencies reported also decrease with absolute percentage point losses of 1.54, 0.79 and 0.07 per order of magnitude, respectively for Cu_2ZnSnS_4, Cu_2ZnGeS_4 and Cu_2ZnSiS_4. The variation of the slopes of the material curves observed in Fig. 5 from one kesterite to another is a direct consequence of the materials optical properties variations. Following the cationic substitution, the variation of the material absorptance function leads to a decrease of the radiative recombination rate value. As a consequence, for lower value of $R_{\text{rad},0}$, a variation of Q_i implies a smaller variation of the non-radiative recombination rate and consequently of the total recombination rate. In addition, any increase of the saturation current density J_0 will lead to a decrease of the open circuit voltage and consequently of the efficiency. Combining these two explanations, as the material absorptance gets optimal with respect to the black body spectrum (i. e., from Cu_2ZnSiS_4 to Cu_2ZnSnS_4), the larger the radiative recombination rate is, the larger the efficiency variation per decade of Q_i will be (see supplementary material). Then, following the variation of the slope observed, for a fixed efficiency value (for example 15%), Cu_2ZnSnS_4 appears more "robust" to larger non-radiative recombination rate as the Q_i value required to reach this efficiency is lower for Cu_2ZnSnS_4 than for Cu_2ZnGeS_4. This highlights the fact that even for a lower ratio of radiative over total recombination rates, a same efficiency is obtained. This tendency is reversed for Q_i value lower than 10^{-5}.

As shown in Fig. 6, the short circuit current density J_{SC} is independent of Q_i as this one is related to the total number of electron-hole pair (EHP) generated by photons absorption (see supplementary material). This quantity depends only on the absorptance of the materials. Following the cationic substitution, the J_{SC} value decreases as the absorptance function worsen with respect to the solar spectrum. In opposition, an increase of the open circuit voltage is observed as the cation is substituted. Indeed, as the optical properties degrades, the radiative recombination rate decreases and consequently the V_{OC} value increases. In addition V_{OC} is Q_i dependent. For a given material, as Q_i tends towards a null value, the total recombination rate will increase resulting in a de-

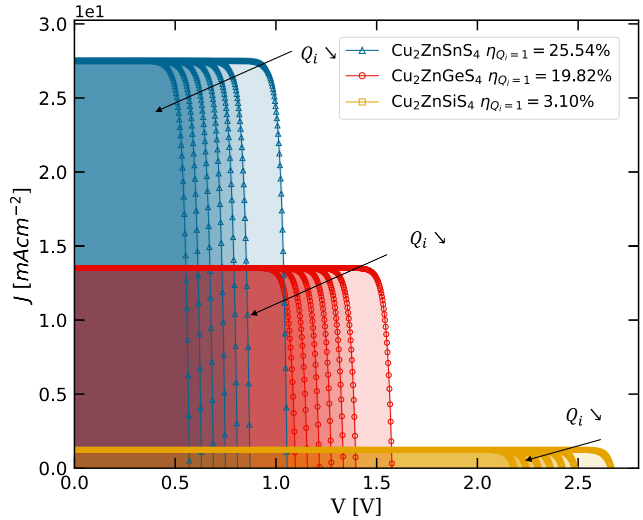

Figure 6. Current density-voltage curves of solar cell modelling for various internal quantum efficiency $Q_i \in [10^{-6}; 1]$. Results obtained for an absorber layer thickness of 1.5 μm.

crease of the V_{OC} value, leading to the decrease of the cell efficiency as reported in Fig. 5. Finally, the differences in η between the three kesterite materials are associated to the decreasing value of J_{SC} which is not fully compensated by the increase of the V_{OC} both attributed to the poorer absorptance as we move from the Sn-containing compound to the Si-containing compound.

In Table 3, we report the electrical solar cell characteristics for each kesterite material incorporated as the absorber layer with the optimal thickness d_{opt} and for an internal quantum efficiency Q_i. Focusing on the results obtained using DFT-calculated reflectivity $R(E)$ and using an internal quantum efficiency of $Q_i = 10^{-4}$ giving open circuit voltage value comparable to experimental ones [9], solar cell efficiencies of 15.88, 14.98 and 2.66 % are reported respectively for Cu_2ZnSnS_4, Cu_2ZnGeS_4 and Cu_2ZnSiS_4(for an optimal thickness of 1.15 μm). In comparison to efficiency values obtained for vanishing radiative recombination rate (25.71, 19.85 and 3.1 % respectively for the Sn-, Ge- and Si-kesterite), one can observe a percentage point loss of nearly 10 for the Sn-compound (4.86 and 0.44 for the Ge- and Si-compound respectively). Then, experimentally, lower J_{SC} values around 21.5 mAcm^{-2} and smaller fill factors values between 60 and 65 % are reported [9]. This observation highlights that the predictions realised with this model corresponds to upper limits. Indeed, nor the materials reflectivity or the absorption of the solar cell upper layers are taken into account, leading to an overestimation of J_{SC}. Concerning the fill factor, the electrical behaviour of the electrodes is assumed to be ideal. By repeating

Materials	E_G [eV]	$R(E)$	Q_i	d_{opt} [μm]	J_{SC} [mAcm^{-2}]	V_{OC} [V]	FF [%]	η [%]	Exp.	Theo.
Cu_2ZnSnS_4	1.32	0	1	2.68	35.69	1.06	88.62	33.38	[9]	[36, 59]
		0	10^{-4}	1.15	35.21	0.70	84.56	20.78		
		DFT	1	2.68	27.68	1.06	88.54	25.71		
		DFT	10^{-4}	1.15	27.19	0.70	84.39	15.88		
Cu_2ZnGeS_4	1.89	0	1	2.02	17.62	1.58	91.65	25.95	[23]	[23, 30, 51]
		0	10^{-4}	1.15	17.53	1.23	89.82	19.65		
		DFT	1	2.02	13.55	1.58	91.59	19.85		
		DFT	10^{-4}	1.15	13.45	1.22	89.73	14.98		
Cu_2ZnSiS_4	3.06	0	1	1.53	1.61	2.67	94.58	4.03	N.A.	N.A.
		0	10^{-4}	1.15	1.60	2.32	93.88	3.46		
		DFT	1	1.53	1.24	2.66	94.55	3.10		
		DFT	10^{-4}	1.15	1.23	2.31	93.85	2.66		

Table 3. Kesterite Cu_2ZnXS_4 (X=Sn,Ge,Si)-based solar cell efficiency modelling using the theoretical model proposed by Blank *et.al.* [36]. Short circuit current density J_{SC}, open circuit voltage V_{OC}, fill factor FF and cell efficiency η values are presented. For each calculation, the optimal absorber layer thickness d_{opt} has been precalculated and then used as parameter. Results are presented for an internal quantum efficiency $Q_i = 1$ and $Q_i = 10^{-4}$ for experimentally comparable V_{OC} values. In order to highlight the impact of the materials reflectivity $R(E)$, the calculation have been performed both for $R(E) = 0$ and for $R(E)$ values as obtained using DFT calculations.

the calculation with a fixed short circuit current density matching the experimental value, a cell efficiency of 12.29 % is reported as well as a V_{OC} value of 685 mV. This result is in good agreement with the values reported experimentally.

Using this methodology, we confirmed the interest regarding Cu_2ZnSnS_4 for single-junction solar cell and we highlight a possible efficiency improvement of nearly 10 % which might be achieved by reducing the non-radiative recombination rate. Then, Cu_2ZnGeS_4 might be interesting as top cell for tandem approaches [23, 60] as this material provides higher bandgap value and interesting cell efficiencies, whereas, Cu_2ZnSiS_4 might be interesting for solar cell applications as PV windows.

Conclusion

In conclusion, we reported direct bandgap values of 1.32, 1.89 and 3.06 eV and absorption coefficients of the order of 10^4 cm^{-1} for, respectively, Cu_2ZnSnS_4, Cu_2ZnGeS_4 and Cu_2ZnSiS_4. Simultaneously a slight increase of the effective mass values is reported following the sequential substitution. Then, using as input data the optical properties of the materials, the solar cell electrical characteristics are predicted based on an improved version of the Shockley-Queisser model. Optimal absorber layer thicknesses between 1.15 and 2.68 μm are reported and efficiencies of 25.71, 19.85 and 3.10 % are obtained for the kesterite compounds following the cationic substitution and the induced variation of the materials properties. In addition, using optical results, we highlighted the negative impact of the materials reflectivity on the solar cell characteristics. Using a non-radiative recombination rate giving V_{OC} values comparable to actual experimental measurements, we reported a decrease of the solar cell efficiencies to 15.88, 14.98 and 2.66 % respectively for Cu_2ZnSnS_4, Cu_2ZnGeS_4 and Cu_2ZnSiS_4. Pointing out these results as upper limits, by reducing the non-radiative recombination current density, the efficiency of Cu_2ZnSnS_4 and Cu_2ZnGeS_4 could be improved respectively by 9.83 and 4.87 %, putting forward these kesterite compounds as promising absorber layer materials.

Conflicts of interest

There are no conflicts to declare.

Acknowledgments

Computational resources have been provided by the Consortium des Équipements de Calcul Intensif (CÉCI), funded by the Fonds de la Recherche Scientifique de Belgique (F.R.S.-FNRS) under Grant No. 2.5020.11 and by the Walloon Region.

---

* thomas.ratz@uliege.be

[1] P. C. K. Vesborg and T. F. Jaramillo, *Addressing the terawatt challenge: scalability in the supply of chemical elements for renewable energy*, RSC Advances **2**, 7933 (2012).

[2] *Communication from the Commision to the European Parliament, the Council, the European Economic and Social Committee and the Committee of the Regions on the*

2017 list of Critical Raw Materials for the EU, 2017, Accessed: 2020-11-18.

[3] M. Green *et al.*, *Solar cell efficiency tables (version 57)*, Progress in Photovoltaics: Research and Applications **29**, 3 (2021).

[4] M. Nakamura *et al.*, *Cd-free Cu(In,Ga)(Se,S)$_2$ thin-film solar cell with record efficiency of 23.35%*, IEEE Journal of Photovoltaics **9**, 1863 (2019).

[5] S. Giraldo *et al.*, *Progress and perspectives of thin film kesterite photovoltaic technology: a critical Review*, Advanced Materials **31**, 1806692 (2019).

[6] W. Wang *et al.*, *Device characteristics of CZTSSe thin-film solar cells with 12.6% efficiency*, Advanced Energy Materials **4**, 1301465 (2013).

[7] C. Yan *et al.*, *Cu_2ZnSnS_4 solar cells with over 10% power conversion efficiency enabled by heterojunction heat treatment*, Nature Energy **3**, 764 (2018).

[8] T. Todorov *et al.*, *Solution-based synthesis of kesterite thin film semiconductors*, Journal of Physics: Energy **2**, 012003 (2020).

[9] T. Ratz *et al.*, *Physical routes for the synthesis of kesterite*, Journal of Physics: Energy **1**, 042003 (2019).

[10] M. Grossberg *et al.*, *The electrical and optical properties of kesterites*, Journal of Physics: Energy **1**, 044002 (2019).

[11] C. Platzer-Björkman *et al.*, *Back and front contacts in kesterite solar cells: state-of-the-art and open questions*, Journal of Physics: Energy **1**, 044005 (2019).

[12] A. Crovetto and O. Hansen, *What is the band alignment of $Cu_2ZnSn(S,Se)_4$ solar cells ?*, Solar Energy Materials and Solar Cells **169**, 177 (2017).

[13] S. Chen, A. Walsh, X.-G. Gong, and S.-H. Wei, *Classification of lattice defects in the kesterite Cu_2ZnSnS_4 and $Cu_2ZnSnSe_4$ earth-abundant solar cell absorbers*, Advanced Materials **25**, 1522 (2013).

[14] S. Kim, J.-S. Park, and A. Walsh, *Identification of killer defects in kesterite thin-film solar cells*, ACS Energy Letters **3**, 496 (2018).

[15] Y. E. Romanyuk *et al.*, *Doping and alloying of kesterites*, Journal of Physics: Energy **1**, 044004 (2019).

[16] J. Li, D. Wang, X. Li, Y. Zeng, and Y. Zhang, *Cation substitution in Earth-abundant kesterite photovoltaic materials*, Advanced Science **5**, 1700744 (2018).

[17] M. S. Kumar, S. P. Madhusudanan, and S. K. Batabyal, *Substitution of Zn in Earth-Abundant $Cu_2ZnSn(S,Se)_4$ based thin film solar cells–A status review*, Solar Energy Materials and Solar Cells **185**, 287 (2018).

[18] C. Tablero, *Electronic and optical properties of substitutional V, Cr and Ir impurities in Cu_2ZnSnS_4*, Solar Energy Materials and Solar Cells **125**, 8 (2014).

[19] S. Kim, K. M. Kim, H. Tampo, H. Shibata, and S. Niki, *Improvement of voltage deficit of Ge-incorporated kesterite solar cell with 12.3% conversion efficiency*, Applied Physics Express **9**, 102301 (2016).

[20] S. Giraldo *et al.*, *How small amounts of Ge modify the formation pathways and crystallization of kesterites*, Energy & Environmental Science **11**, 582 (2018).

[21] M. Buffière *et al.*, *Physical characterization of $Cu_2ZnGeSe_4$ thin films from annealing of Cu-Zn-Ge precursor layers*, Thin Solid Films **582**, 171 (2015).

[22] L. Choubrac *et al.*, *7.6% CZGSe solar cells thanks to optimized CdS chemical bath deposition*, Physica Status Solidi (a) **215**, 1800043 (2018).

[23] B. Vermang *et al.*, *Wide band gap kesterite absorbers for thin film solar cells: potential and challenges for their deployment in tandem devices*, Sustainable Energy & Fuels **3**, 2246 (2019).

[24] S. Khelifi *et al.*, *The path towards efficient wide band gap thin-film kesterite solar cells with transparent back contact for viable tandem application*, Solar Energy Materials and Solar Cells **219**, 110824 (2021).

[25] S. Chen *et al.*, *Wurtzite-derived polytypes of kesterite and stannite quaternary chalcogenide semiconductors*, Physical Review B **82**, Part (2010).

[26] S. Zamulko, R. Chen, and C. Persson, *Investigation of the structural, optical and electronic properties of $Cu_2Zn(Sn,Si/Ge)(S/Se)_4$ alloys for solar cell applications*, Physica Status Solidi (b) **254**, 1700084 (2017).

[27] H.-R. Liu *et al.*, *First-principles study on the effective masses of zinc-blend-derived $Cu_2ZnIVVI_4$ (IV = Sn, Ge, Si and VI = S, Se)*, Journal of Applied Physics **112**, 093717 (2012).

[28] C. Dun, N. Holzwarth, Y. Li, W. Huang, and D. L. Carroll, *$Cu_2ZnSn(S_xO_{(1-x)})_4$ and $Cu_2ZnSn(S_xSe_{(1-x)})_4$: First principles simulations of optimal alloy configurations and their energies*, Journal of Applied Physics **115**, 193513 (2014).

[29] A. Walsh, S. Chen, S.-H. Wei, and X.-G. Gong, *Kesterite thin-film solar cells: Advances in materials modelling of Cu_2ZnSnS_4*, Advanced Energy Materials **2**, 400 (2012).

[30] J. Jiang *et al.*, *Inserting an intermediate band in Cu- and Ag-based Kesterite compounds by Sb doping: A first-principles study*, Materials Science and Engineering: B **264**, 114937 (2021).

[31] J. Paier, R. Asahi, A. Nagoya, and G. Kresse, *Cu_2ZnSnS_4 as a potential photovoltaic material: a hybrid Hartree-Fock density functional theory study*, Physical Review B **79**, 115126 (2009).

[32] Y. Zhang *et al.*, *Structural properties and quasiparticle band structures of Cu-based quaternary semiconductors for photovoltaic applications*, Journal of Applied Physics **111**, 063709 (2012).

[33] G. K. Gupta, R. Chaurasiya, and A. Dixit, *Theoretical studies on structural, electronic and optical properties of kesterite and stannite $Cu_2ZnGe(S/Se)_4$ solar cell absorbers*, Computational Condensed Matter **19**, e00334 (2019).

[34] W. Shockley and H. J. Queisser, *Detailed balance limit of efficiency of p-n junction solar cells*, Journal of Applied Physics **32**, 510 (1961).

[35] J. Heyd, G. E. Scuseria, and M. Ernzerhof, *Hybrid functionals based on a screened Coulomb potential*, The Journal of Chemical Physics **118**, 8207 (2003).

[36] B. Blank, T. Kirchartz, S. Lany, and U. Rau, *Selection metric for photovoltaic materials screening based on detailed-balance analysis*, Physical Review Applied **8**, 024032 (2017).

[37] G. Kresse and J. Furthmüller, *Efficiency of ab-initio total energy calculations for metals and semiconductors using a plane-wave basis set*, Computational Materials Science **6**, 15 (1996).

[38] G. Kresse and D. Joubert, *From ultrasoft pseudopotentials to the projector augmented-wave method*, Physical Review B **59**, 1758 (1999).

[39] J. P. Perdew, K. Burke, and M. Ernzerhof, *Generalized gradient approximation made simple*, Physical Review Letters **77**, 3865 (1996).

[40] J. Sun, A. Ruzsinszky, and J. P. Perdew, *Strongly constrained and appropriately normed semilocal density functional*, Physical Review Letters **115**, 036402 (2015).

[41] J. Sun *et al.*, *Accurate first-principles structures and energies of diversely bonded systems from an efficient density functional*, Nature Chemistry **8**, 831 (2016).

[42] D. Fritsch and S. Schorr, *Climbing Jacob's ladder: A density functional theory case study for $Ag_2ZnSnSe_4$ and $Cu_2ZnSnSe_4$*, Journal of Physics: Energy **3**, 015002 (2020).

[43] J. Heyd, J. E. Peralta, G. E. Scuseria, and R. L. Martin, *Energy band gaps and lattice parameters evaluated with the Heyd-Scuseria-Ernzerhof screened hybrid functional*, The Journal of Chemical Physics **123**, 174101 (2005).

[44] Q. Guo, H. W. Hillhouse, and R. Agrawal, *Synthesis of Cu_2ZnSnS_4 nanocrystal ink and its use for solar cells*, Journal of the American Chemical Society **131**, 11672 (2009).

[45] S. Levcenko, V. Tezlevan, E. Arushanov, S. Schorr, and T. Unold, *Free-to-bound recombination in near stoichiometric Cu_2ZnSnS_4 single crystals*, Physical Review B **86**, 045206 (2012).

[46] K. Lisunov *et al.*, *Features of the acceptor band and properties of localized carriers from studies of the variable-range hopping conduction in single crystals of p-Cu_2ZnSnS_4*, Solar Energy Materials and Solar Cells **112**, 127 (2013).

[47] J. Chen, W. Li, C. Yan, S. Huang, and X. Hao, *Studies of compositional dependent $Cu_2Zn(Ge_xSn_{1-x})S_4$ thin films prepared by sulfurizing sputtered metallic precursors*, Journal of Alloys and Compounds **621**, 154 (2015).

[48] S. Schorr, H.-J. Hoebler, and M. Tovar, *A neutron diffraction study of the stannite-kesterite solid solution series*, European Journal of Mineralogy **19**, 65 (2007).

[49] K. Tsuji, T. Maeda, and T. Wada, *Optical properties and electronic structures of Cu_2ZnSnS_4, Cu_2ZnGeS_4, and $Cu_2Zn(Ge,Sn)S_4$ and $Cu_2Zn(Ge,Sn)Se_4$ solid solutions*, Japanese Journal of Applied Physics **57**, 08RC21 (2018).

[50] D. B. Khadka and J. Kim, *Study of structural and optical properties of kesterite Cu_2ZnGeX_4 (X= S, Se) thin films synthesized by chemical spray pyrolysis*, CrystEngComm **15**, 10500 (2013).

[51] M. Courel, T. Sanchez, N. Mathews, and X. Mathew, *Cu_2ZnGeS_4 thin films deposited by thermal evaporation: the impact of Ge concentration on physical properties*, Journal of Physics D: Applied Physics **51**, 095107 (2018).

[52] M. Hamdi *et al.*, *Crystal chemistry and optical investigations of the $Cu_2Zn(Sn,Si)S_4$ series for photovoltaic applications*, Journal of Solid State Chemistry **220**, 232 (2014).

[53] S. Levcenco *et al.*, *Polarization-dependent electrolyte electroreflectance study of Cu_2ZnSiS_4 and $Cu_2ZnSiSe_4$ single crystals*, Journal of Alloys and Compounds **509**, 7105 (2011).

[54] J. C. Slater, *Atomic radii in crystals*, The Journal of Chemical Physics **41**, 3199 (1964).

[55] C. P. Heinrich, T. W. Day, W. G. Zeier, G. J. Snyder, and W. Tremel, *Effect of Isovalent Substitution on the Thermoelectric Properties of the $Cu_2ZnGeSe_{4-x}S_x$ Series of Solid Solutions*, Journal of the American Chemical Society **136**, 442 (2014).

[56] S. Ikeda *et al.*, *Photocathode characteristics of a spray-deposited Cu_2ZnGeS_4 thin film for CO_2 reduction in a CO_2-saturated aqueous solution*, ACS Applied Energy Materials **2**, 6911 (2019).

[57] E. Garcia-Llamas *et al.*, *Wide band-gap tuning $Cu_2ZnSn_{1-x}Ge_xS_4$ single crystals: Optical and vibrational properties*, Solar Energy Materials and Solar Cells **158**, 147 (2016).

[58] M. Vishwakarma, D. Varandani, S. Shivaprasad, and B. Mehta, *Structural, optical, electrical properties and energy band diagram of Cu_2ZnSiS_4 thin films*, Solar Energy Materials and Solar Cells **174**, 577 (2018).

[59] S. Kim, J. A. Márquez, T. Unold, and A. Walsh, *Upper limit to the photovoltaic efficiency of imperfect crystals from first principles*, Energy & Environmental Science **13**, 1481 (2020).

[60] I. El Radaf and H. Al-Zahrani, *Facile Synthesis and Structural, Linear and Nonlinear Optical Investigation of p-type Cu_2ZnGeS_4 Thin Films as a Potential Absorber Layer for Solar Cells*, Journal of Electronic Materials **49**, 4843 (2020).